Journal of Power Sources 196 (2011) 235–245

Contents lists available at ScienceDirect

Journal of Power Sources

journal homepage: www.elsevier.com/locate/jpowsour

Transient characteristics of proton exchange membrane fuel cells with different flow field designs

Hung-Yi Li [a,*], Wen-Chung Weng [a], Wei-Mon Yan [b,**], Xiao-Dong Wang [c]

[a] Department of Mechatronic Engineering, Huafan University, Shihtin, Taipei 22301, Taiwan
[b] Department of Greenergy, National University of Tainan, Tainan 70005, Taiwan
[c] Department of Thermal Engineering, University of Science & Technology Beijing, Beijing 100083, China

ARTICLE INFO

Article history:
Received 22 April 2010
Received in revised form 14 June 2010
Accepted 15 June 2010
Available online 23 June 2010

Keywords:
Flow field design
Voltage loading effect
Transient characteristics
Transient response time
Undershoot
Overshoot

ABSTRACT

This work establishes three-dimensional transient numerical models of proton exchange membrane fuel cells (PEMFCs) with different cathode flow field designs. Exactly how flow field design and voltage loading affect the transient characteristics of the PEMFCs are examined. When the operating voltage instantaneously drops from 0.7 V to 0.5 V, the electrochemical reactions increase. To ensure sufficient oxygen supply for the fuel cell, the oxygen mass fractions are high in the cathode gas diffusion and cathode catalyst layers, causing overshoot of the local current density distribution. When the operating voltage suddenly increases from 0.5 V to 0.7 V, the electrochemical reactions become mild, and furthermore the oxygen mass fraction distribution becomes low, leading to undershoot of the local current density distribution. The transient response time required to reach the steady state for the parallel flow field with baffle design is longest in the event of overshoot or undershoot among the different cathode flow field designs. The overshoot or undershoot phenomena become more obvious with larger voltage loading variations. Moreover, the transient response time for the Z-type flow field with baffle design is longer than for the Z-type flow field design.

1. Introduction

Numerical models have been establishing extensively to understand the physical phenomena and steady state or transient characteristics of proton exchange membrane fuel cells (PEMFCs). They possess the advantage of reducing the costs and time involved in research and development, offering easy comparison with experimental data, and enabling the calculation of physical quantities that are hard or impossible to measure.

Most studies on the numerical simulation of fuel cells emphasize the steady state characteristics of one-dimensional [1,2], two-dimensional [3–6], and three-dimensional [7–12] models. Flow field design [13–16] and parameter design [17–21] have attracted considerable interest.

Pertinent literature reviews demonstrate that numerical simulations of steady state characteristics of fuel cells are well established. However, transient characteristics of fuel cells have received limited attention [22–39]. Transient load changes during operation of PEMFCs often occur in stationary or automotive applications, for example a sudden variation of load as a device starts or as a vehicle is accelerated or decelerated. The current density overshoots its final steady state value when the operating voltage changes abruptly from high to low; by contrast, the current density undershoots its final steady state value when the operating voltage changes abruptly from low to high. The transient response times for the overshoot and undershoot phenomena to reach steady states are important to evaluate the dynamic performance of PEMFCs. Thus, numerical models capable of investigating the transient characteristics are needed in the analysis of PEMFCs, when the operating conditions vary with time. Amphlett et al. [22] developed a transient model for predicting transient characteristics of proton exchange membrane fuel cells. Moreover, Yan et al. [29] designed two-dimensional transient numerical models of proton exchange membrane fuel cells to examine the transient transport characteristics and system performance of the PEMFCs. The study found that with increasing channel width fraction, porosity of the gas diffusion layer and surface over-potential of the catalyst layer reduces the transient response time. Kumar and Reddy [32] demonstrated a clear effect of flow field design on the steady state and transient performance of the polymer electrolyte membrane fuel cell. Their investigation studied four different flow field designs, namely serpentine, parallel, multi-parallel and interdigitated. The parallel design exhibited the highest transient response. Mean-

* Corresponding author. Tel.: +886 2 26632102x4017; fax: +886 2 26632102x4013.
** Corresponding author. Tel.: +886 6 2602251; fax: +886 6 2602205.
E-mail addresses: hyli@huafan.hfu.edu.tw (H.-Y. Li), wmyan@mail.nutn.edu.tw (W.-M. Yan).

0378-7753/$ – see front matter © 2010 Elsevier B.V. All rights reserved.
doi:10.1016/j.jpowsour.2010.06.047

Nomenclature

Aj_0^{ref}	reference exchange current density ($A\,m^{-3}$)
C	mass fraction
C_F	quadratic drag factor
D	mass diffusivity ($m^2\,s^{-1}$)
F	Faraday constant (96,487 $C\,mol^{-1}$)
i	current density ($A\,m^{-2}$)
I	average current density ($A\,m^{-2}$)
j	transfer current density ($A\,m^{-3}$)
k_c	coefficient of water vapor condensation rate (s^{-1})
k_e	coefficient of water vapor evaporation rate ($atm^{-1}\,s^{-1}$)
k_p	permeability (m^2)
M	molecular weight ($kg\,mol^{-1}$)
p	pressure (atm)
n_d	electro-osmotic drag coefficient
R	universal gas constant (8.314 $J\,mol^{-1}\,K^{-1}$)
s	saturation of liquid water
S_c	source term in the species equation
S_j	source term in the electric potential equation
S_L	source term due to phase change of water
$S_{\vec{u}}$	source term in the momentum equation
T	temperature (K)
t	time (s)
$\vec{u}$	velocity ($m\,s^{-1}$)
V_{cell}	operating voltage (V)
x, y, z	coordinates (m)

Greek symbols

α_a	electrical transfer coefficient in forward reaction
α_c	electrical transfer coefficient in backward reaction
ε	porosity
η	over-potential (V)
λ	water content in the membrane
ρ	density ($kg\,m^{-3}$)
σ_m	ionic conductivity ($\Omega^{-1}\,m^{-1}$)
σ_s	electronic conductivity ($\Omega^{-1}\,m^{-1}$)
μ	dynamic viscosity (Pa s)
τ	tortuosity of the pores in the porous material
Φ_m	electric potential of the ionic phase (V)
Φ_s	electric potential of the electronic phase (V)

Subscripts and superscripts

a	anode
c	cathode
ch	channel
CL	catalyst layer
eff	effective value
k	kth species of the mixture
GDL	gas diffusion layer
g	gas
H_2	hydrogen
H_2O	water
l	liquid
m	membrane
O_2	oxygen
sat	saturation
ref	reference value

while, the interdigitated design exhibited the slowest transient response. Guilin and Jianren [38] established a three-dimensional, transient, non-isothermal and single-phase CFD model of a proton exchange membrane fuel cell with a serpentine channel to describe the transient process and dynamic characteristics of the PEMFC.

The literature on transient characteristics of fuel cells focused mainly on one-dimensional or two-dimensional models with parallel or serpentine flow field. Therefore, this study establishes three-dimensional computational models of the proton exchange membrane fuel cells with five different flow field designs, namely parallel flow field, Z-type flow field, serpentine flow field, parallel flow field with baffle and Z-type flow field with baffle. Finally, the effects of voltage loading on the transient response time, local current density distribution, oxygen mass fraction distribution and hydrogen mass fraction distribution for the different flow field designs are discussed.

2. Analysis

This study establishes three-dimensional transient numerical models of PEMFCs with five different flow field designs using the finite volume method. The flow field designs in the PEMFCs include the parallel flow field, Z-type flow field, serpentine flow field, parallel flow field with baffle and Z-type flow field with baffle, as illustrated in Fig. 1. The transient characteristics of the PEMFCs are examined by analyzing the electrochemical reactions and transport phenomena of the reactants and products in the PEMFCs.

The fuel cell comprises the anode gas flow field, anode gas diffusion layer, anode catalyst layer, proton exchange membrane, cathode catalyst layer, cathode gas diffusion layer, and cathode gas flow field. The governing equations for the analysis include mass, momentum, species and electric potential equations. The following assumptions are made: the cell system is isothermal; the reactants and products are ideal gases; the flow is laminar and incompressible; the electrochemical reactions only occur in the catalyst layer; the porous layers, such as the gas diffusion layer, catalyst layer and proton exchange membrane, are isotropic. The fuel cell has dimensions 2.3 cm × 2.3 cm × 2.645 cm. Furthermore, the width and height of the flow field are 1 mm in all cases. The thicknesses of the diffusion layer, catalyst layer and proton exchange membrane are set to 0.3 mm, 0.005 mm and 0.035 mm, respectively. Finally, the fuel cell temperature is assumed to be 323 K.

Given the above assumptions, the governing equations are as follows.

Continuity equation:

$$\frac{\partial\left(\varepsilon_{eff}\rho_g\right)}{\partial t} + \nabla\cdot\left(\varepsilon_{eff}\rho_g\vec{u}_g\right) = -S_L \tag{1}$$

where ε_{eff} denotes the effective porosity of the porous material, ρ_g represents the density of the gaseous mixture and $\vec{u}_g$ is the velocity of the gaseous mixture.

Momentum equation:

$$\frac{\varepsilon}{(1-s)}\frac{\partial\left(\rho_g\vec{u}_g\right)}{\partial t} + \frac{\varepsilon}{(1-s)^2}\nabla\cdot\left(\rho_g\vec{u}_g\vec{u}_g\right) = -\varepsilon\nabla p_g + \frac{\varepsilon}{(1-s)}\nabla\cdot\left(\mu_g\nabla\vec{u}_g\right) + S_{\vec{u}} \tag{2}$$

where ε denotes the porosity of the porous material, s represents the saturation of liquid water, defined as the ratio of liquid water volume to pore volume in the porous material, p_g is the pressure of the gas mixture, μ_g denotes the dynamic viscosity of the gas mixture, $S_{\vec{u}}$ represents the source term based on the Darcy drag force imposed by the pore wall on the fluid, which generally causes a significant pressure drop across the porous material, and is represented by

$$S_{\vec{u}} = -\frac{\varepsilon^2\mu_g\vec{u}_g}{k_p k_{rg}} - \frac{\varepsilon^3 C_F\rho_g}{\sqrt{k_p}}\left|\vec{u}_g\right|\vec{u}_g \tag{3}$$

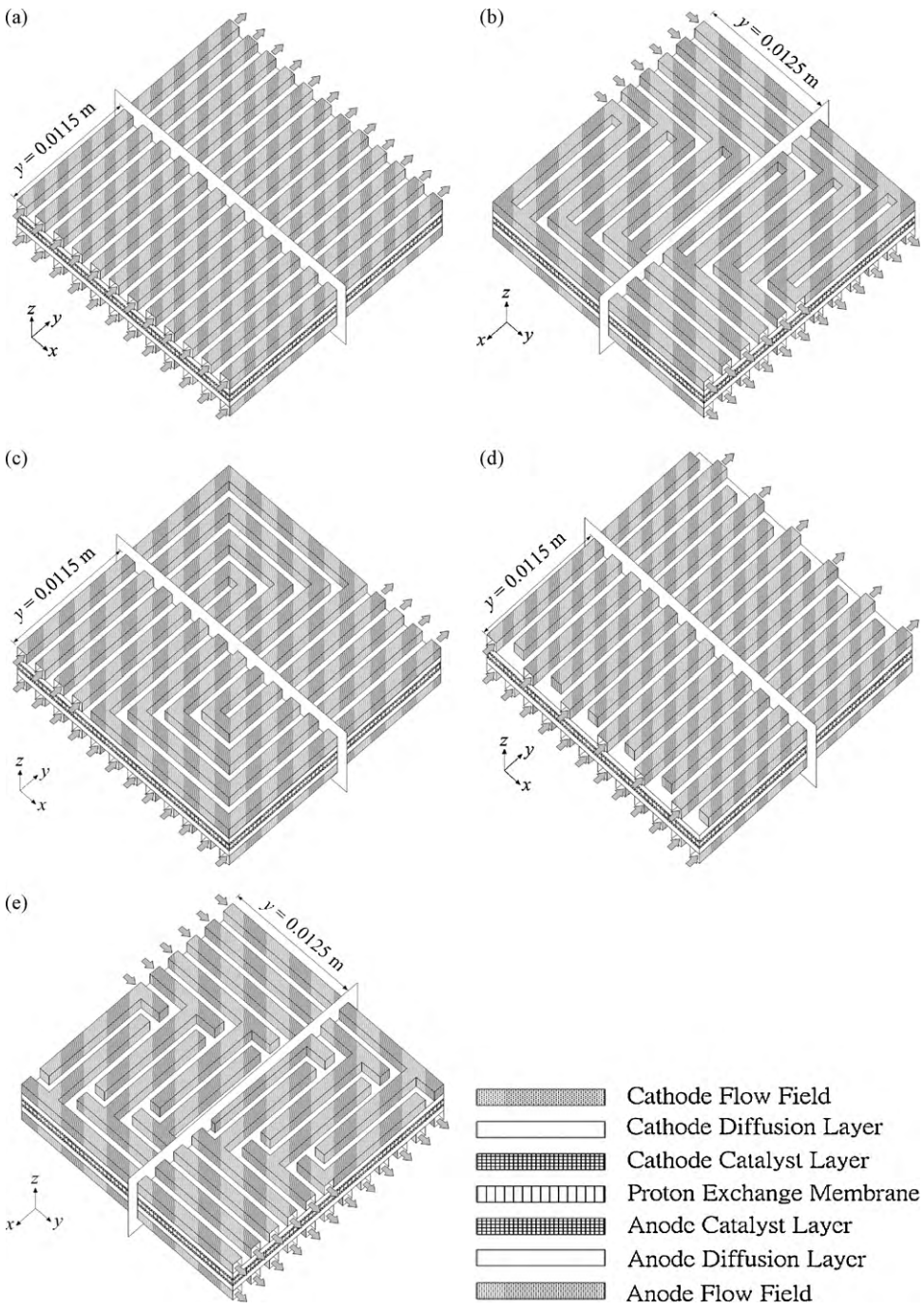

Fig. 1. Numerical models of the PEMFCs with different flow field designs: (a) parallel flow field, (b) Z-type flow field, (c) serpentine flow field, (d) parallel flow field with baffle and (e) Z-type flow field with baffle.

In Eq. (3), k_{rg} denotes the relative permeability of the gaseous mixture given by $k_{rg} = (1-s)^3$, C_F represents the quadratic drag factor, and k_p is the permeability of the porous material. The relationship between the porosity and permeability is expressed by the Blake–Kozeny equation [40]

$$k_P = \left(\frac{d_{porous}^2}{150}\right)\left[\frac{\varepsilon^3}{(1-\varepsilon)^2}\right] \quad (4)$$

where d_{porous} denotes the equivalent pore diameter of the porous material.

Species equation:

$$\frac{\partial\left(\varepsilon_{eff}\rho_g C_k\right)}{\partial t} + \nabla\cdot\left(\varepsilon_{eff}\rho_g \vec{u}_g C_k\right) = \nabla\cdot\left(\rho_g D_{k,eff}\nabla C_k\right) + S_c - S_L \quad (5)$$

where C_k represents the mass fraction of the kth species and $D_{k,eff}$ is the effective mass diffusivity of the kth species. The Bruggemann equation [15] indicates the influence of the porosity on the mass diffusivity.

$$D_{k,eff} = D_k \varepsilon_{eff}^{\tau} \quad (6)$$

In the catalyst layer, the source term in the species equation, S_c, represents the source term that produced by the electrochemical

reaction, which differs among the various reactants, for example S_c is $-(j_a/2F)M_{H_2}$ for hydrogen, $-(j_c/4F)M_{O_2}$ for oxygen, and $(j_c/2F)M_{H_2O}$ for water vapor. The parameters j_a and j_c denote the transfer current densities on the anode and cathode sides, which can be calculated using the Butler–Volmer equations [3].

$$j_a = Aj_{0,a}^{ref}\left(\frac{C_{H_2}}{C_{H_2}^{ref}}\right)^{1/2}\left[e^{(\alpha_a F/RT)\eta} - \frac{1}{e^{(\alpha_c F/RT)\eta}}\right] \quad (7)$$

$$j_c = Aj_{0,c}^{ref}\left(\frac{C_{O_2}}{C_{O_2}^{ref}}\right)\left[e^{(\alpha_a F/RT)\eta} - \frac{1}{e^{(\alpha_c F/RT)\eta}}\right] \quad (8)$$

where $Aj_{0,a}^{ref}$ and $Aj_{0,c}^{ref}$ represent the reference exchange current densities at the anode and cathode, α_a, and α_c are the electrical transfer coefficients, F denotes the Faraday constant, R represents the universal gas constant, T is the fuel cell temperature and η denotes the over-potential.

The potential equation is used to calculate the electric potential and electric current produced by the electrochemical reactions. The current density includes the ionic current density, $\vec{i}_m$, and electronic current density, $\vec{i}_s$. The equation for current conservation is as follows [7]

$$\nabla\cdot\vec{i}_m + \nabla\cdot\vec{i}_s = 0 \quad (9)$$

From Ohm's law, the following two equations are obtained:

$$\nabla\cdot(\sigma_m\nabla\Phi_m) = S_j \quad (10)$$

$$\nabla\cdot(\sigma_s\nabla\Phi_s) = -S_j \quad (11)$$

where σ_m denotes the ionic conductivity, σ_s represents the electronic conductivity, Φ_m is the electric potential of the ionic phase, Φ_s denotes the electric potential of the electronic phase, and S_j is the source term, which is zero in the PEM without electrochemical reaction and $-j_a$ or $-j_c$ on the anode or cathode sides. The ionic conductivity is calculated using [41,42]

$$\sigma_m = \sigma_m^{ref}\exp\left[1268\left(\frac{1}{303} - \frac{1}{T}\right)\right] \quad (12)$$

where the membrane reference conductivity σ_m^{ref} is given by

$$\sigma_m^{ref} = 0.005139\lambda - 0.326 \quad (13)$$

In the flow channels, gas diffusion layers and catalyst layers, the equation governing liquid water transport and formation is expressed using the generalized Richards equation.

$$\frac{\partial(\varepsilon\rho_l s)}{\partial t} + \nabla\cdot\left(\frac{\rho_l k_p k_{rl}}{\mu_l}\frac{\partial p_c}{\partial s}\nabla s\right) - \nabla\cdot\left(\frac{\rho_l k_p k_{rl}}{\mu_l}\nabla p_g\right) + \nabla\cdot\left(\frac{n_d M_{H_2O}}{F}\vec{i}_m\right) = S_L \quad (14)$$

where ρ_l denotes the density of liquid water, μ_l represents the dynamic viscosity of liquid water, p_c is the capillary pressure, M_{H_2O} denotes the molecular weight of water, k_{rl} represents the relative permeability of liquid water, and n_d is the electro-osmotic drag coefficient.

When the partial pressure of the water vapor exceeds its saturation pressure, the water vapor is assumed to condense and fill the pores in the porous material. The source term, S_L, is evaluated using [8]

$$S_L = \begin{cases} M_{H_2O}k_c\dfrac{\varepsilon(1-s)x_{H_2O}}{RT}\left(p_{H_2O} - p_{sat}\right) & \text{if } p_{H_2O} > p_{sat} \\ k_e\varepsilon s\rho_l\left(p_{H_2O} - p_{sat}\right) & \text{if } p_{H_2O} < p_{sat} \end{cases} \quad (15)$$

where k_c denotes the condensation rate constant of water, k_e represents the evaporation rate constant of water, x_{H_2O} is the mole fraction of water vapor, and p_{sat} denotes the saturation pressure of water vapor calculated by

$$p_{sat} = 10^{-2.1794+0.02953T-9.1837\times10^{-5}T^2+1.4454\times10^{-7}T^3} \quad (16)$$

Assuming water exists only as liquid phase in the membrane, the liquid water transport equation in the membrane can be expressed as

$$\frac{\partial\left(\rho_{dry}M_{H_2O}\lambda/M_m\right)}{\partial t} + \nabla\cdot\left(\left(\frac{\alpha_d M_{H_2O}}{F}\vec{i}_m\right)\lambda - \left(\frac{M_{H_2O}\rho_{dry}}{M_m}D_\lambda\right)\nabla\lambda\right) = 0 \quad (17)$$

where ρ_{dry} denotes the membrane dry density, M_m represents the membrane equivalent weight, α_d is a constant, and D_λ denotes the diffusivity.

The boundary conditions in the anode and cathode flow channels are as follows: the inlet flow rates are 65 $cm^3\,min^{-1}$ and 175 $cm^3\,min^{-1}$ on the anode and cathode sides, respectively. Furthermore, the inlet reactants on the anode side included hydrogen with relative humidity of 100%, the inlet reactants on the cathode side contained air with a relative humidity of 100%, and the flows are fully developed at the outlets of the anode and cathode flow channels. The solid walls are assumed to be no slip with zero fluxes. At the interfaces between the gas channels, diffusion layers, catalyst layers, and PEM, the velocities, mass fractions, momentum fluxes, and mass fluxes are all assumed to be equal. Table 1 lists the model parameters. The initial condition is obtained as the steady state solution using these parameters and a given operating voltage.

Three non-uniform distributed grid configurations, namely (I) $x\times y\times z = 70\times70\times40$, (II) $x\times y\times z = 93\times93\times47$ and (III) $x\times y\times z = 116\times116\times54$, are employed to determine whether the solutions are independent of the mesh. Fig. 2(a) shows the effect of the grid number on the *I–V* curve of the fuel cell. The *I–V* curves obtained using grid configurations (II) and (III) display little difference. Furthermore, the relative error in current density is 0.19% at operating voltage 0.3 V. However, the difference in the *I–V* curves obtained using grid configurations (I) and (III) is larger and the relative error in current density is 6.23% at operating voltage 0.3 V. The relative error is defined as the absolute value of the difference between the

Table 1
The fuel cell parameters (Gurau et al. [3], Mazumder and Cole [7,8]).

Parameter	Quantity
ε_{ch}	1
ε_{GDL}	0.5
ε_{CL}	0.4
ε_m	0.28
$k_{p,ch}$	∞
$k_{p,GDL}$	1.76×10^{-10} m^2
$k_{p,CL}$	1.76×10^{-11} m^2
$k_{p,m}$	1.8×10^{-18} m^2
τ_{ch}	1
τ_{GDL}	1.5
τ_{CL}	1.5
τ_m	Dagan model
$Aj_{0,a}^{ref}$	9.227×10^8 $A\,m^{-3}$
$Aj_{0,c}^{ref}$	1.05×10^6 $A\,m^{-3}$
α_a/α_c (anode)	0.5/0.5
α_a/α_c (cathode)	1.5/1.5
k_c	100 s^{-1}
k_e	100 $atm^{-1}\,s^{-1}$
σ_s	5000 $\Omega^{-1}\,m^{-1}$
$\sigma_{m,CL}$	4.2 $\Omega^{-1}\,m^{-1}$
ρ_l	1000 $kg\,m^{-3}$
ρ_{dry}	1980 $kg\,m^{-3}$
μ_l	3.65×10^{-4} Pa s
M_m	1.1 $kg\,mol^{-1}$

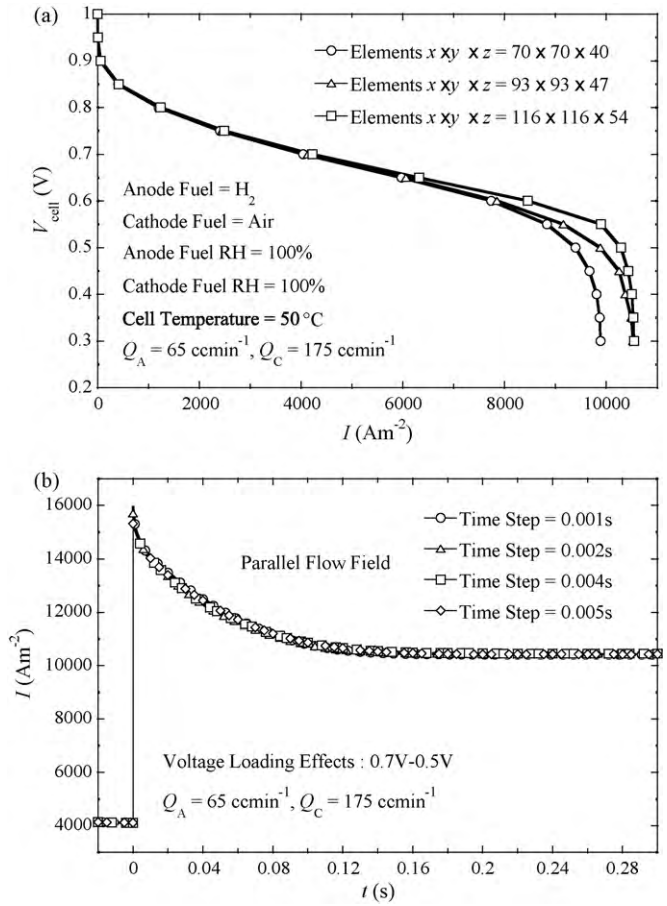

Fig. 2. Grid point and time step tests: (a) grid point and (b) time step.

calculated value and the exact value divided by the exact value. The mesh with $x \times y \times z = 93 \times 93 \times 47$ is used to achieve a tradeoff between computational effort and accuracy. Fig. 2(b) shows the effect of the time step on the current density of the fuel cell when the operating voltage undergoes a step change from 0.7 V to 0.5 V at $t = 0$. Notably, the predicted current densities are close for the time steps of 0.001 s, 0.002 s, 0.004 s and 0.005 s. Thus, this study adopts the time step of 0.002 s.

The accuracy of the steady state version of the present numerical model was demonstrated by Yan et al. [43]. Fig. 3 shows a comparison of the calculated transient current density distributions with the results by Wang et al. [44]. It is found that the current density distributions are almost overlapped when the operating voltage is 0.7 V. Additionally, the average relative error in the current density distribution is 7.26% for the parallel flow field and 3.93% for the parallel flow field with baffle when the operating voltage is 0.5 V. Hence, it is adequate to use the three-dimensional transient numerical model for analyzing the dynamic performance of the PEMFCs.

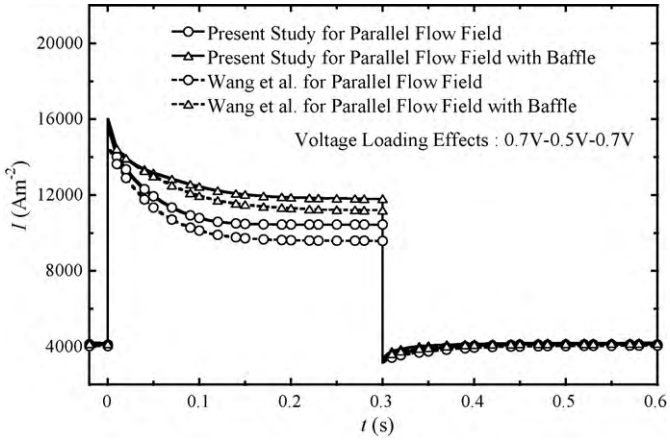

Fig. 3. Comparison of the calculated transient current density distributions with the results by Wang et al. [44].

3. Results and discussion

The transport characteristics of the fuel and moving rates of the liquid water are different for proton exchange membrane fuel cells with different flow field designs. Thus, the flow field design significantly influences the steady state performance of the PEMFCs, indicating that different flow field designs may influence the transient characteristics of the PEMFCs. This study investigates the transient characteristics of proton exchange membrane fuel cells with five different cathode flow field designs, namely parallel flow field, Z-type flow field, serpentine flow field, parallel flow field with baffle and Z-type flow field with baffle. Specifically, the effects of the flow field design and voltage loading on the transient response time, local oxygen and hydrogen mass fraction distributions and current density distribution are analyzed.

3.1. Effects of cathode flow field design on transient characteristics of proton exchange membrane fuel cells

Fig. 4 illustrates the effects of the dynamic voltage loading on the cell performance of the PEMFCs with different cathode flow field designs. Fig. 4(a) shows the V_{cell}–t curve of the PEMFCs

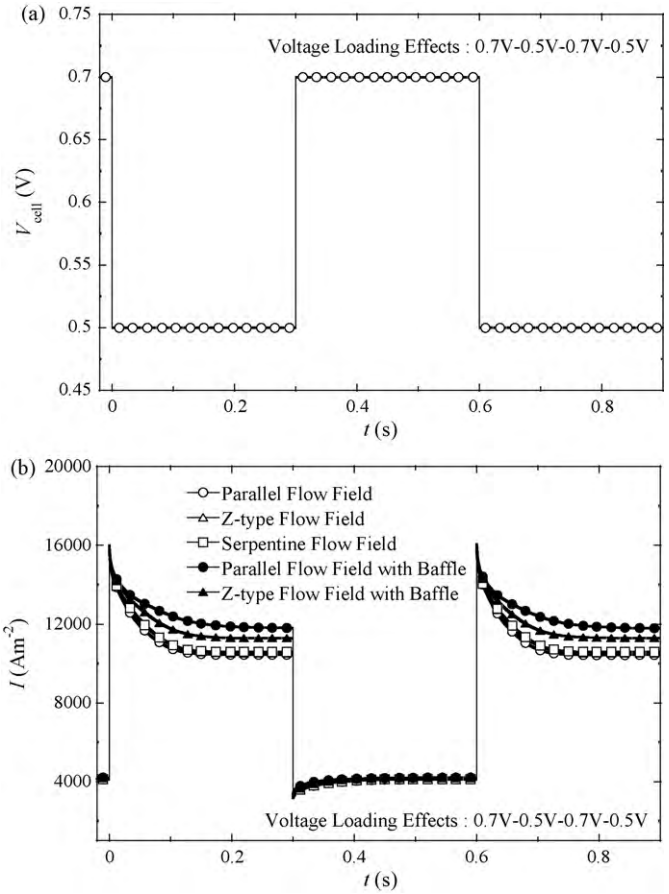

Fig. 4. Effects of dynamic voltage loading on the cell performance of PEMFCs with different cathode flow field designs: (a) dynamic voltage loading and (b) dynamic response of cell performance.

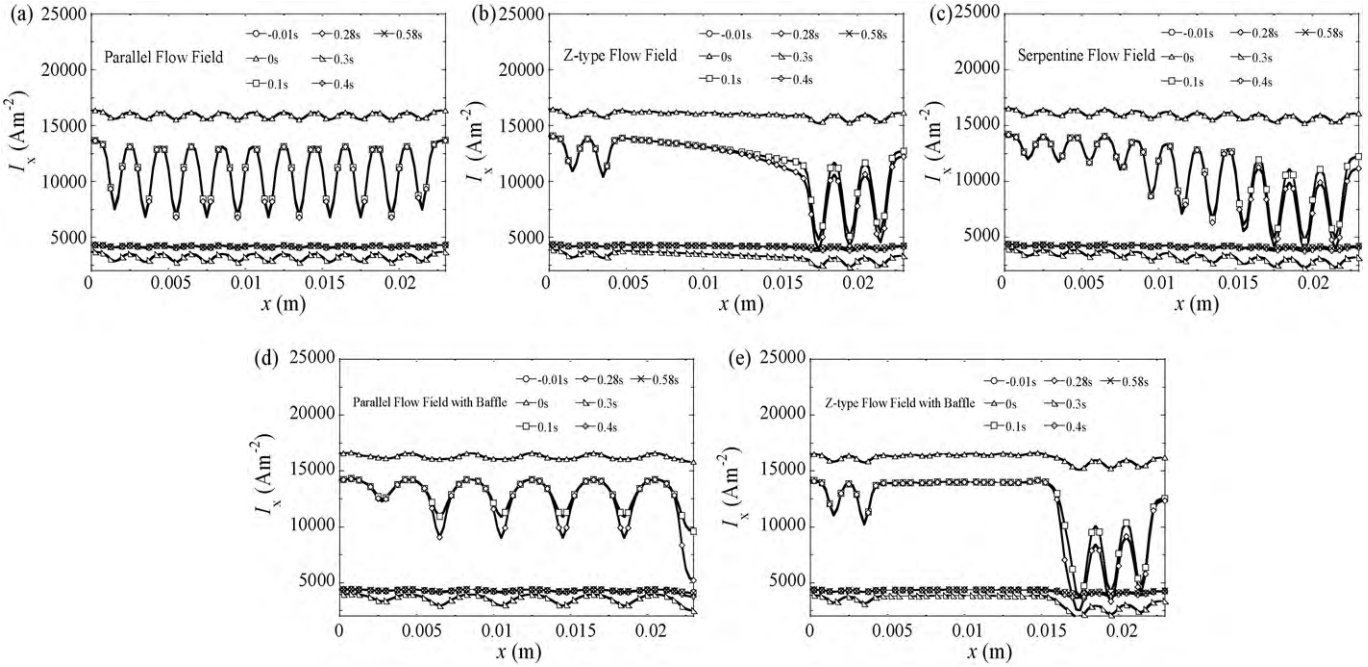

Fig. 5. Local current density distributions at different times at the middle of the PEM along the *x* axis for different flow field designs: (a) parallel flow field, (b) Z-type flow field, (c) serpentine flow field, (d) parallel flow field with baffle, and (e) Z-type flow field with baffle.

where $V_{cell} = 0.7$ V for $t < 0$ s, $V_{cell} = 0.5$ V for $0\text{ s} \le t < 0.3$ s, $V_{cell} = 0.7$ V for $0.3\text{ s} \le t < 0.6$ s, and $V_{cell} = 0.5$ V for $0.6\text{ s} \le t$. The voltage loading exhibits three step changes between 0.5 V and 0.7 V at $t = 0$ s, 0.3 s and 0.6 s, with the voltage loading decreasing at $t = 0$ s and 0.6 s, and increasing at $t = 0.3$ s, respectively. Fig. 4(b) shows the *I*–*t* curves of the PEMFCs. The fuel cell operates at a steady state corresponding to $V_{cell} = 0.7$ V for $t < 0$ s, and the PEMFCs with the five cathode flow field designs all exhibit similar cell performance. At $t = 0$ s, the operating voltage decreases suddenly from 0.7 V to 0.5 V. Additionally, the current density increases abruptly and overshoot occurs, then the current density decreases slowly before achieving a steady state. The transient response time required for this overshoot to reach the steady state is 0.17 s for the parallel flow field, 0.174 s for the Z-type flow field, 0.188 s for the serpentine flow field, 0.266 s for the parallel flow field with baffle, and 0.214 s for the Z-type flow field with baffle. At $t = 0.3$ s, the operating voltage increases rapidly from 0.5 V to 0.7 V. The current density decreases abruptly and undershoot occurs, then the current density increases slowly and stabilizes. The transient response time required for the undershoot to reach the steady state is 0.198 s for the parallel flow field, 0.198 s for the Z-type flow field, 0.19 s for the serpentine flow field, 0.232 s for the parallel flow field with baffle, and 0.212 s for the Z-type flow field with baffle. To summarize, the variation of the current density is largest and the transient response time is longest for the parallel flow field with baffle in instances of overshoot or undershoot.

Fig. 5 shows the local current density distributions at different times at the middle of the PEM along the *x* direction for different cathode flow field designs. At $t = -0.01$ s, the operating voltage is 0.7 V and the electrochemical reactions are mild. The local current density distributions differ little among different flow field designs. At $t = 0$ s, the operating voltage reduces from 0.7 V to 0.5 V, and thus the electrochemical reactions become strong and the local current density distribution increases markedly. The local current densities differ little under the channels and ribs. The local current density distribution is larger than that corresponding to the steady state for an operating voltage of 0.5 V and overshoot occurs. At $t = 0.1$ s, the local current density distribution is smaller than at $t = 0$ s. Additionally, the local current densities under the ribs decrease more significant increasing the differences in the local current densities under the channels and ribs. The local current density distribution is comparatively uniform for the parallel flow field with baffle among the five flow field designs. The local current density distributions differ little between $t = 0.28$ s and 0.1 s, suggesting that the steady state is reached. At $t = 0.3$ s, the operating voltage increases from 0.5 V to 0.7 V, and thus the local current density distribution becomes small. The differences in the local current densities under the channels and ribs exceed those at $t = 0.4$ s. Moreover, the local current density distribution is less than that corresponding to the steady state for an operating voltage of 0.7 V, and undershoot occurs. At $t = 0.58$ s, the local current density distribution almost overlaps with that at $t = 0.4$ s, implying that the fuel cell reaches a steady state.

Fig. 6 shows the oxygen mass fraction distributions at different times at the middle of the interface of the cathode diffusion and catalytic layers along the *x* axis for different flow field designs. At $t = -0.01$ s, the cell voltage is 0.7 V and the electrochemical reactions are mild. Consequently, the oxygen consumption is small and the oxygen mass fraction distribution remains high and uniform under the channels and ribs. At $t = 0$ s, the operating voltage decreases suddenly from 0.7 V to 0.5 V. Because the oxygen mass fraction distribution is high and the electrochemical reactions become strong, the local current density distribution increases markedly and exceeds the steady state value at 0.5 V, resulting in overshoot. The supply of the high and uniform oxygen mass fraction distribution under the channels and ribs also increases the uniformity of the local current density distribution. Thus it can be inferred that the overshoot results from the high and uniform oxygen mass fraction distribution when the operating voltage immediately changes from high to low. The PEMFC with the parallel flow field with baffle possesses a higher oxygen mass fraction distribution among the five different flow designs, and thus exhibits more obvious overshoot behavior. At $t = 0.1$ s, the local oxygen mass fraction distribution is lower than at $t = 0$ s and exhibits higher variation under the channels and ribs, leading to a less uniform local current density distribution. At $t = 0.28$ s, the oxygen mass fraction distribution

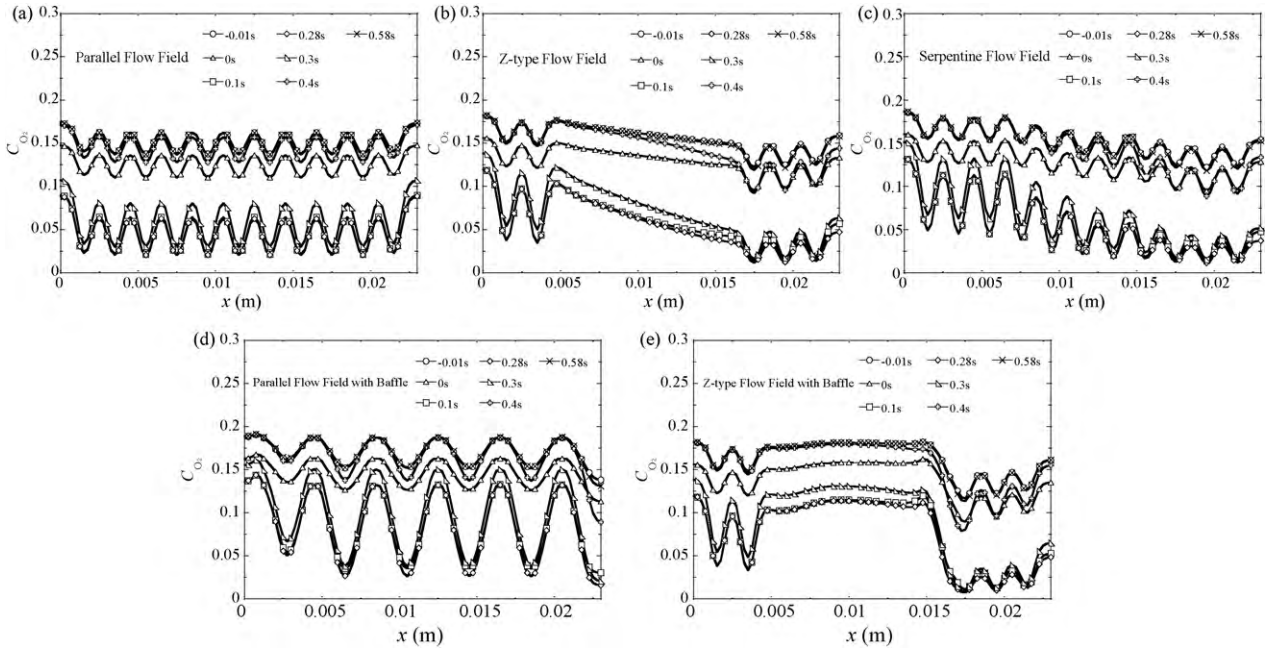

Fig. 6. Oxygen mass fraction distributions at different times at the middle of the interface of the cathode diffusion and catalytic layers along the *x* axis for different flow field designs: (a) parallel flow field, (b) Z-type flow field, (c) serpentine flow field, (d) parallel flow field with baffle, and (e) Z-type flow field with baffle.

almost overlaps with that at $t = 0.1$ s, implying that the fuel cell reaches a steady state. At $t = 0.3$ s, the operating voltage increases from 0.5 V to 0.7 V, and thus the electrochemical reactions become mild. The oxygen mass fraction distribution is lower than for the steady state at 0.7 V. Hence, the local current density distribution is lower than for the steady state value at an operating voltage of 0.7 V, and undershoot thus occurs. Moreover, the oxygen mass fraction distribution is less uniform under the channels and ribs, implying that the undershoot phenomena result from the lower and non-uniform oxygen mass fraction distribution when the operating voltage instantly changes from low to high. The PEMFC using the parallel flow field with baffle possesses a lower oxygen mass fraction distribution among the five different flow designs, and thus exhibits more obvious undershoot behavior. At $t = 0.4$ s, the oxygen mass fraction distribution exceeds that at $t = 0.3$ s. Additionally, the distributions under the channels and ribs do not differ obviously. At $t = 0.58$ s the oxygen mass fraction distribution almost overlaps with that at $t = 0.4$ s, implying the approaching of a steady state. To summarize, the oxygen mass fraction distribution critically influences the overshoot or the undershoot phenomena and the current

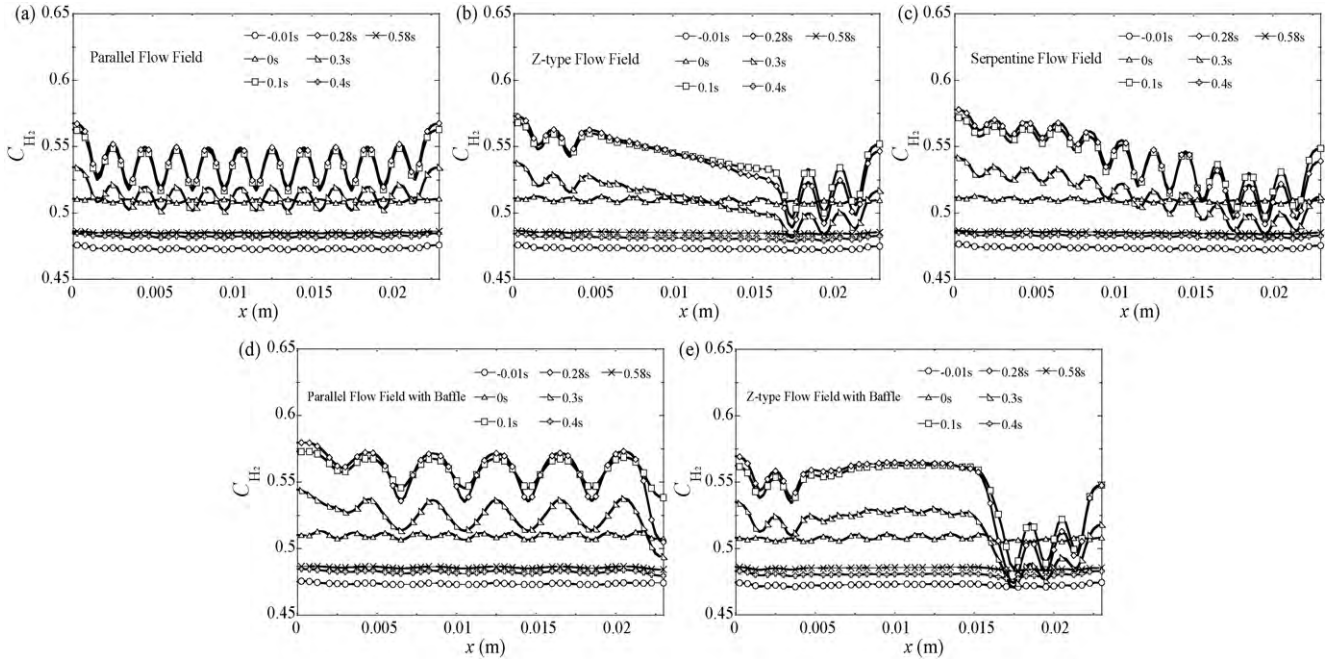

Fig. 7. Hydrogen mass fraction distributions at different times at the middle of the interface of the anode diffusion and catalytic layers along the *x* axis for different flow field designs: (a) parallel flow field, (b) Z-type flow field, (c) serpentine flow field, (d) parallel flow field with baffle, and (e) Z-type flow field with baffle.

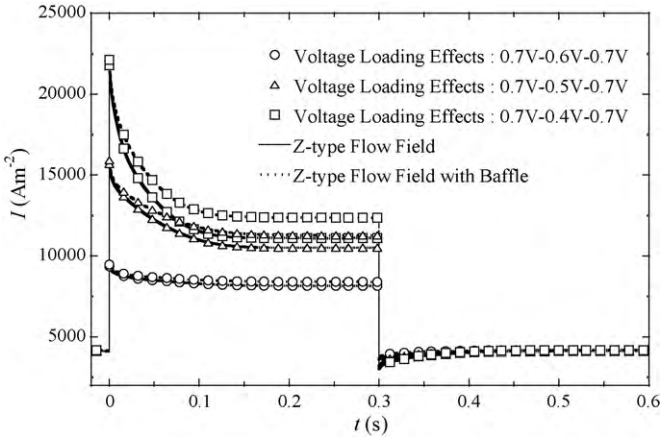

Fig. 8. Variation of current density over time for different voltage loadings.

density distribution of the PEMFCs with different cathode flow field designs.

Fig. 7 illustrates the hydrogen mass fraction distributions at different times at the middle of the interface of the anode diffusion and catalytic layers along the x direction for different flow field designs. At $t = -0.01$ s, the operating voltage is 0.7 V and the electrochemical reactions are mild. Consequently, hydrogen consumption is low and the hydrogen mass fraction distribution remains uniform. At $t = 0$ s, the operating voltage reduces suddenly from 0.7 V to 0.5 V. Although the electrochemical reaction is severe and the consumption of hydrogen increases, the water movement along with the proton from the anode to the cathode owing to the electro-osmotic drag effect also increases. The numerical results demonstrate that the local hydrogen mass fraction distribution exceeds that at $t = -0.01$ s. With the continuation of the electrochemical reactions and the process of water formation and transport, the hydrogen mass fraction distribution at $t = 0.1$ s becomes much higher than at $t = 0$ s. At $t = 0.28$ s the hydrogen mass fraction distribution does not overlap with but slightly exceeds that at $t = 0.1$ s. Thus, the hydrogen mass fraction distribution does not reach a steady state. At $t = 0.3$ s, the operating voltage increases from 0.5 V to 0.7 V, and thus the electrochemical reactions become mild. Hydrogen consumption decreases, and so too does the amount of liquid water moving from the anode to the cathode. The numerical results show that the hydrogen mass fraction distribution decreases significantly. At $t = 0.58$ s, the hydrogen mass fraction distribution is much lower than that at $t = 0.3$ s. Furthermore, the distribution remains very uniform for all cathode flow channel designs. The operating voltage is 0.7 V at −0.01 s and 0.58 s. However, the hydrogen mass fraction distributions clearly differ at −0.01 s and 0.58 s for any cathode flow field design, indicating that the hydrogen mass fraction distribution does not stabilize, and is not directly related to the overshoot or undershoot.

3.2. Effects of voltage loading on transient characteristics of proton exchange membrane fuel cells

The above discussion demonstrates that the cathode flow field designs significantly influence the transient response time and overshoot or undershoot. The subsequent section investigates the effects of the voltage loading on the transient characteristics of the proton exchange membrane fuel cells using the Z-type flow field and Z-type flow field with baffle. Different dynamic voltage loadings are applied to examine their effects on the transient local current density distribution and oxygen mass fraction distribution of the proton exchange membrane fuel cells.

Fig. 8 shows the variation of the current density over time given changing voltage loadings, including $V_{cell} = 0.7$ V for $t < 0$ s, $V_{cell} = 0.6$ V, 0.5 V or 0.4 V for $0\text{ s} \le t < 0.3$ s and $V_{cell} = 0.7$ V for $0.3\text{ s} \le t < 0.6$ s. When $t < 0$ s, the operating voltage is 0.7 V and the electrochemical reactions are mild. The current density distributions are close for different flow field designs. The overshoot of the current density is clearer when the operating voltage decreases from 0.7 V to 0.4 V at $t = 0$ s than when it decreases to 0.5 V or 0.6 V. This difference arises because the electrochemical reactions are stronger and the increase in the current density is greater when the decrease in the operating voltage is larger. Additionally, the overshoot of the current density is larger for the Z-type flow field with baffle than for the Z-type flow field. Over time, the current density decreases slowly and reaches a steady state. The time required to reach the steady state is 0.16 s, 0.174 s and 0.188 s for the Z-type flow field when the operating voltage decreases from 0.7 V to 0.6 V, 0.5 V or 0.4 V, respectively. Meanwhile, the time required to reach the steady state is 0.206 s, 0.214 s and 0.234 s for the Z-type flow field with baffle when the operating voltage decreases from 0.7 V to 0.6 V, 0.5 V or 0.4 V, respectively. Moreover, the current density is higher for the Z-type flow field with baffle than the Z-type flow field because the former offers better water removal and fuel utilization. The undershoot of the current density is larger when the operating voltage increases from 0.4 V to 0.7 V at $t = 0.3$ s than when it increases from just 0.5 V or 0.6 V. This is because the decreases in the electrochemical reactions and current density are clearer when the increase in the operating voltage is larger, resulting in larger undershoot. The undershoot of the current density is clearer for the Z-type flow field with baffle than for the Z-type flow field. Over time, the current density slowly increases and reaches a steady state. The time taken to reach the steady state is 0.18 s, 0.188 s and 0.204 s for the Z-type flow field with operating voltage increasing from 0.6 V, 0.5 V or 0.4 V to 0.7 V, respectively. Furthermore, the time taken to reach the steady state is 0.188 s, 0.212 s and 0.222 s for the Z-type flow field with baffle when the operating voltage increases from 0.6 V, 0.5 V or 0.4 V to 0.7 V, respectively. To summarize, the overshoot or undershoot are more significant and the transient response time is longer when the variation of the operation voltage is larger for the Z-type flow field with baffle.

Fig. 9 displays the local current density distributions at different times at the middle of the PEM along the x axis when the voltage loading changes with $V_{cell} = 0.7$ V for $t < 0$ s, $V_{cell} = 0.6$ V, 0.5 V or 0.4 V for $0\text{ s} \le t < 0.3$ s and $V_{cell} = 0.7$ V for $0.3\text{ s} \le t < 0.6$ s. At $t = -0.01$ s, the operating voltage is 0.7 V and the electrochemical reactions are mild, resulting in a relatively uniform local current density distribution. At $t = 0$ s, the operating voltage drops suddenly from 0.7 V to 0.6 V, 0.5 V or 0.4 V. The electrochemical reactions intensify and the local current density distribution increases markedly. Furthermore, the variation of the current density under the channels and ribs is not obvious. The increase and overshoot of the current density distribution is more obvious when the operating voltage decreases from 0.7 V to 0.4 V at $t = 0$ s than when it decreases to 0.5 V or 0.6 V. The local current density distribution is smaller at $t = 0.1$ s than at $t = 0$ s for the Z-type flow field or the Z-type flow field with baffle. As the scale of the drop in the operating voltage increases, the local current density distribution becomes less uniform. The decrease in the local current density distribution becomes more obvious under the ribs than under the channels. The local current density distribution at $t = 0.28$ s is almost identical to that at $t = 0.1$ s, indicating that a steady state is being approached. At $t = 0.3$ s, the operating voltage suddenly increases to 0.7 V, leading to a low local current density distribution. The differences in local current density distribution under the channels and ribs exceed those at $t = 0.4$ s. Moreover, the undershoot of the local current density distribution shows that values are smaller than the steady state values corresponding to the operating voltage of 0.7 V. The local current density distribution at

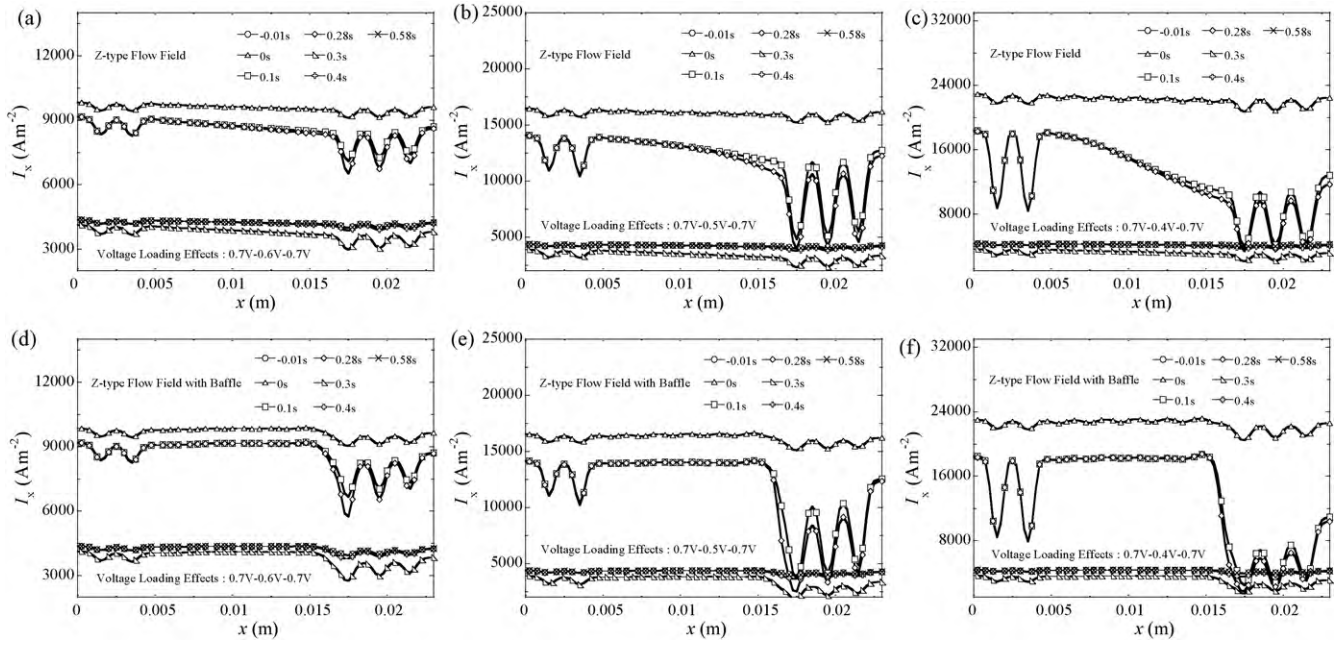

Fig. 9. Local current density distributions at different times at the middle of the PEM along the x axis for different voltage loadings: (a and d) decreases from 0.7 V to 0.6 V then increases to 0.7 V, (b and e) decreases from 0.7 V to 0.5 V then increases to 0.7 V, and (c and f) decreases from 0.7 V to 0.4 V then increases to 0.7 V.

$t = 0.58$ s is almost identical to that at $t = 0.4$ s, indicating the arrival of a steady state.

Fig. 10 presents the oxygen mass fraction distributions at different times at the middle of the interface of the cathode diffusion and catalytic layers along the x axis when the voltage loading changes with $V_{cell} = 0.7$ V for $t < 0$ s, $V_{cell} = 0.6$ V, 0.5 V or 0.4 V for $0\text{ s} \le t < 0.3$ s and $V_{cell} = 0.7$ V for $0.3\text{ s} \le t < 0.6$ s. At $t = -0.01$ s, the operating voltage is 0.7 V and the electrochemical reactions are mild. Therefore, the oxygen consumption is low and the oxygen mass fraction distribution is high for both flow field designs. At $t = 0$ s, the operating voltage decreases suddenly from 0.7 V to 0.6 V, 0.5 V or 0.4 V. The electrochemical reactions are strong and the oxygen consumption significantly increases. The increase in oxygen consumption grows with the decrease in operating voltage. At $t = 0.1$ s, the oxygen mass fraction distribution is lower than that at $t = 0$ s. Moreover, the differences in the oxygen mass fraction distribution under the channels and ribs are clearer when the operating voltage drops from 0.7 V to 0.4 V than when it drops to 0.5 V or 0.6 V. The oxygen mass fraction distribution at $t = 0.28$ s is almost the same as at $t = 0.1$ s, suggesting that a steady state is being reached. At $t = 0.3$ s, the operating voltage suddenly increases to 0.7 V, and hence the electrochemical reactions weaken and the oxygen mass

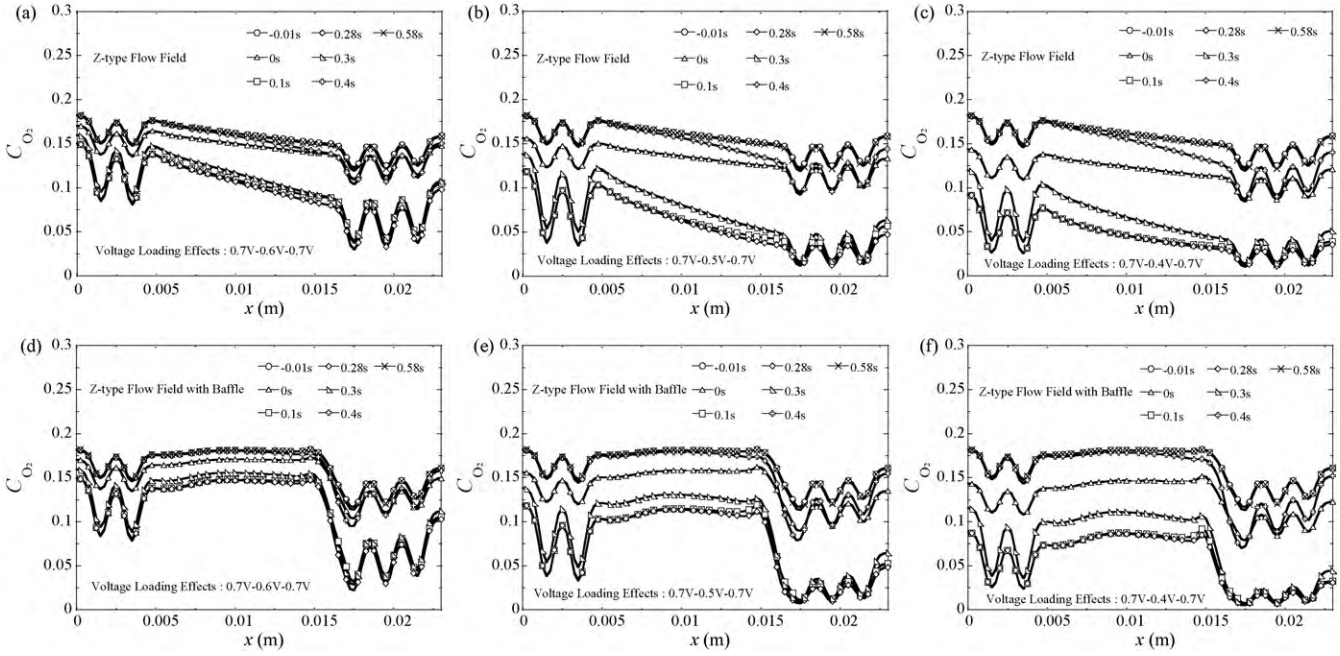

Fig. 10. Oxygen mass fraction distributions at different times at the middle of the interface of the cathode diffusion and catalytic layers along the x axis for different voltage loadings: (a and d) decreases from 0.7 V to 0.6 V then increases to 0.7 V, (b and e) decreases from 0.7 V to 0.5 V then increases to 0.7 V, and (c and f) decreases from 0.7 V to 0.4 V then increases to 0.7 V.

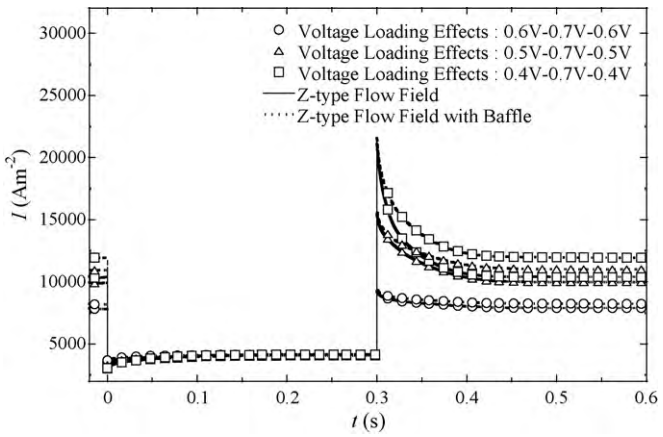

Fig. 11. Variation of current density over time for different voltage loadings.

fraction distribution increases. Furthermore, the oxygen mass fraction distribution increases with the operating voltage. At $t = 0.4$ s, the oxygen mass fraction distribution exceeds that at $t = 0.3$ s. The oxygen mass fraction distribution at $t = 0.58$ s is almost the same as at $t = 0.4$ s, indicating the arrival of a steady state.

Fig. 11 plots the variation of the current density over time given changing voltage loadings, including $V_{cell} = 0.6$ V, 0.5 V or 0.4 V for $t < 0$ s, $V_{cell} = 0.7$ V for $0\text{ s} \leq t < 0.3$ s and $V_{cell} = 0.6$ V, 0.5 V or 0.4 V for $0.3\text{ s} \leq t < 0.6$ s. When $t < 0$ s, the operating voltage is low and the electrochemical reactions are strong. The local current density distribution increases with low operating voltage. The Z-type flow field with baffle provides better water removal and fuel utilization than the Z-type flow field. Therefore, the current density distribution of the Z-type flow field with baffle is higher. The undershoot of the current density is clearer when the operating voltage increases from 0.4 V to 0.7 V at $t = 0$ s than when it increases from 0.5 V or 0.6 V. This phenomenon occurs because the electrochemical reactions are mild at 0.7 V and the current density decreases more given a large increase in operating voltage. Over time, the current density increases slowly and reaches a steady state. The time taken to reach the steady state is 0.2 s, 0.216 s and 0.222 s for the Z-type flow field when the operating voltage increases from 0.6 V, 0.5 V or 0.4 V to 0.7 V, respectively. The time taken to reach the steady state is 0.212 s, 0.23 s and 0.238 s for the Z-type flow field with baffle when the operating voltage increases from 0.6 V, 0.5 V or 0.4 V to 0.7 V, respectively. When $t = 0.3$ s the operating voltage decreases from 0.7 V to 0.4 V, 0.5 V or 0.6 V, intensifying the electrochemical reactions. The overshoot of the current density is more obvious with a larger decrease in operating voltage. Additionally, the overshoot of the current density is clearer for the Z-type flow field with baffle than for Z-type flow field. Over time, the current density slowly decreases and reaches a steady state. The time taken to obtain the steady state is 0.16 s, 0.176 s and 0.188 s for the Z-type flow field when the operating voltage decreases from 0.7 V to 0.6 V, 0.5 V or 0.4 V, respectively. Meanwhile, the time taken to obtain the steady state is 0.206 s, 0.228 s and 0.232 s for the Z-type flow field with baffle when the operating voltage decreases from 0.7 V to 0.6 V, 0.5 V or 0.4 V, respectively. Hence, the overshoot or undershoot phenomena are more significant and the transient response time is longer given larger variation of operating voltage and the use of a Z-type flow field with baffle.

4. Conclusions

This study numerically investigates the transient characteristics of the PEMFCs with five cathode flow field designs. The effects of voltage loading on the transient behavior and local fuel mass fraction distribution are analyzed to understand the overshoot and undershoot phenomena involving the current density. This study concludes the following.

1. When the operating voltage is at a steady value of 0.7 V, the electrochemical reactions are mild, and hence the local current density distributions do not differ clearly among different flow field designs.
2. When the operating voltage reduces from 0.7 V to 0.5 V instantaneously, overshoot of the current density distribution results from the high and uniform oxygen mass fraction distribution. The parallel flow field with baffle design has the highest oxygen mass fraction distribution among the five cathode flow field designs due to the rapid variation in voltage. Thus, the overshoot phenomena are clearest and the transient response time is longest for the parallel flow field with baffle design.
3. When the operating voltage suddenly increases from 0.5 V to 0.7 V, undershoot of the current density distribution results from the low and non-uniform oxygen mass fraction distribution. The parallel flow field with baffle design has the lowest oxygen mass fraction distribution among the five cathode flow field designs owing to the prompt voltage variation. Thus, the undershoot phenomena are clearest and the transient response time is longest for the parallel flow field with baffle design.
4. Ranked in decreasing order of time taken for the overshoot of the local current density of the PEMFCs to reach the steady state, the various flow field designs are as follows: parallel flow field with baffle, Z-type flow field with baffle, serpentine flow field, Z-type flow field and parallel flow field. Ranked in increasing order of time taken for the undershoot of the local current density of the PEMFCs to reach the steady state, the various flow field designs are as follows: parallel flow field with baffle, Z-type flow field with baffle, Z-type flow field, parallel flow field and serpentine flow field.
5. The overshoot or undershoot phenomena become clearer given large voltage loading variations. Moreover, the transient response time required to reach the steady state for the Z-type flow field with baffle design exceeds that for the Z-type flow field design.

Acknowledgements

The authors would like to thank the National Science Council for financially supporting this research under Contract No. NSC 95-2221-E-211-020. This study was partially supported by the NSFC (no. 50876009).

References

[1] A. Rowe, X. Li, J. Power Sources 102 (2001) 82–96.
[2] N. Djilali, D. Lu, Int. J. Therm. Sci. 41 (2002) 29–40.
[3] V. Gurau, H. Liu, S. Kakac, AIChE J. 44 (1998) 2410–2422.
[4] L. You, H. Liu, Int. J. Heat Mass Transfer 45 (2002) 2277–2287.
[5] S.H. Ge, B.L. Yi, J. Power Sources 124 (2003) 1–11.
[6] H.C. Liu, W.M. Yan, C.Y. Soong, F. Chen, J. Power Sources 142 (2005) 125–133.
[7] S. Mazumder, J.V. Cole, J. Electrochem. Soc. 150 (2003) A1503–A1509.
[8] S. Mazumder, J.V. Cole, J. Electrochem. Soc. 150 (2003) A1510–A1517.
[9] M. Hu, A. Gu, M. Wang, X. Zhu, L. Yu, Energy Convers. Manage. 45 (2004) 1861–1882.
[10] M. Hu, X. Zhu, M. Wang, A. Gu, L. Yu, Energy Convers. Manage. 45 (2004) 1883–1916.
[11] W. Ying, Y.J. Sohn, W.Y. Lee, J. Ke, C.S. Kim, J. Power Sources 145 (2005) 563–571.
[12] W. Ying, T.H. Yang, W.Y. Lee, J. Ke, C.S. Kim, J. Power Sources 145 (2005) 572–581.
[13] T.V. Nguyen, J. Electrochem. Soc. 143 (1996) L103–L105.
[14] D.L. Wood, J.S. Yi, T.V. Nguyen, Electrochim. Acta 43 (1998) 3795–3809.
[15] W. He, J.S. Yi, T.V. Nguyen, AIChE J. 46 (2000) 2053–2064.
[16] S.W. Cha, R. O'Hayre, Y. Saito, F.B. Prinz, J. Power Sources 134 (2004) 57–71.
[17] H.C. Liu, W.M. Yan, C.Y. Soong, F. Chen, H.S. Chu, J. Power Sources 158 (2006) 78–87.
[18] T. Berning, D.M. Lu, N. Djilali, J. Power Sources 106 (2002) 284–294.

[19] D. Natarajan, T.V. Nguyen, J. Power Sources 115 (2003) 66–80.
[20] P. Berg, K. Promislow, J.S. Pierre, J. Stumper, B. Wetton, J. Electrochem. Soc. 151 (2004) A341–A353.
[21] W.M. Yan, C.Y. Soong, F. Chen, H.S. Chu, J. Power Sources 125 (2004) 27–39.
[22] J.C. Amphlett, R.F. Mann, B.A. Peppley, P.R. Roberge, A. Rodrigues, J. Power Sources 61 (1996) 183–188.
[23] D. Natarajan, T.V. Nguyen, J. Electrochem. Soc. 148 (2001) A1324–A1335.
[24] M. Ceraolo, C. Miulli, A. Pozio, J. Power Sources 113 (2003) 131–144.
[25] S. Yerramalla, A. Davari, A. Feliachi, T. Biswas, J. Power Sources 124 (2003) 104–113.
[26] W. Friede, S. Rael, B. Davat, IEEE Trans. Power Electron. 19 (2004) 1234–1241.
[27] Y. Shan, S.Y. Choe, J. Power Sources 145 (2005) 30–39.
[28] P.R. Pathapati, X. Xue, J. Tang, Renew. Energy 30 (2005) 1–22.
[29] W.M. Yan, C.Y. Soong, F. Chen, H.S. Chu, J. Power Sources 143 (2005) 48–56.
[30] W.M. Yan, H.S. Chu, J.Y. Chen, C.Y. Soong, F. Chen, J. Power Sources 162 (2006) 1147–1156.
[31] Y. Wang, C.Y. Wang, Electrochim. Acta 50 (2005) 1307–1315.
[32] A. Kumar, R.G. Reddy, J. Power Sources 155 (2006) 264–271.
[33] D. Song, Q. Wang, Z.S. Liu, C. Huang, J. Power Sources 159 (2006) 928–942.
[34] S. Shimpalee, W.K. Lee, J.W. Van Zee, H. Naseri-Neshat, J. Power Sources 156 (2006) 355–368.
[35] S. Shimpalee, W.K. Lee, J.W. Van Zee, H. Naseri-Neshat, J. Power Sources 156 (2006) 369–374.
[36] H. Wu, P. Berg, X. Li, J. Power Sources 165 (2007) 232–243.
[37] H. Meng, J. Power Sources 171 (2007) 738–746.
[38] H. Guilin, F. Jianren, J. Power Sources 165 (2007) 171–184.
[39] S. Shimpalee, D. Spuckler, J.W. Van Zee, J. Power Sources 167 (2007) 130–138.
[40] F.A.L. Dullien, Porous Media, Academic Press, New York, 1991.
[41] T.E. Springer, T.A. Zawodzinski, S. Gottesfeld, J. Electrochem. Soc. 138 (1991) 2334–2342.
[42] T.V. Nguyen, R.E. White, J. Electrochem. Soc. 140 (1993) 2178–2186.
[43] W.M. Yan, H.Y. Li, W.C. Tsai, J. Electrochem. Soc. 153 (2006) A1984–A1991.
[44] X.D. Wang, W.M. Yan, X.X. Zhang, G. Lu, A. Su, Int. J. Heat Mass Transfer, submitted for publication.